ACS APPLIED MATERIALS & INTERFACES

Research Article

www.acsami.org

# Amorphous and Crystalline Sodium Tantalate Composites for Photocatalytic Water Splitting

Tobias Grewe and Harun Tüysüz*

Max-Planck-Institute für Kohlenforschung, Kaiser-Wilhelm-Platz 1, 45470 Mülheim an der Ruhr, Germany

Supporting Information

**ABSTRACT:** A facile hydrothermal synthesis protocol for the fabrication of sodium tantalates for photocatalytic water splitting is presented. Mixtures of tantalum and sodium ethoxide precursors were dispersed in ethanol, and ammonium hydroxide solution was used as mineralizer. By adjusting the amount of mineralizer, a variety of sodium tantalates with various morphologies, textural parameters, band gaps, crystal phases, and degrees of crystallinity were fabricated. The reaction was carefully monitored with a pressure sensor inside the autoclave reactor, and the obtained samples were characterized using X-ray diffraction, transmission electron microscopy, $N_2$-physisorption, and ultraviolet−visible light spectroscopy. Among the series, the amorphous sample and the composite sample that consists of amorphous and crystalline phases showed superior activity toward photocatalytic hydrogen production than highly crystalline samples. Particularly, an amorphous sodium tantalate with a small fraction of crystalline nanoparticles with perovskite structure was found to be the most active sample, reaching a hydrogen rate of 3.6 mmol $h^{-1}$ from water/methanol without the use of any cocatalyst. Despite its amorphous nature, this photocatalyst gave an apparent photocatalyst activity of 1200 $\mu$mol $g^{-1}$ $L^{-1}$ $h^{-1}$ $W^{1-}$, which is 4.5-fold higher than highly crystalline $NaTaO_3$. In addition, the most active sample gave promising activity for overall water splitting with a hydrogen production rate of 94 $\mu$mol $h^{-1}$, which is superior to highly crystalline $NaTaO_3$ prepared by conventional solid−solid state route.

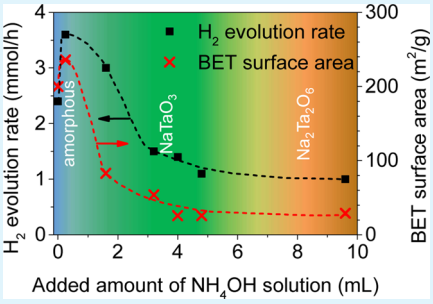


**KEYWORDS:** *solar energy, water splitting, hydrogen production, nanoparticle, amorphous*

## INTRODUCTION

Solar energy conversion into chemical energy via photocatalytic water splitting is one of the most promising long-term strategies toward sustainable energy and meeting worldwide energy demands since it produces clean hydrogen as a dense fuel.[1,2] The design of novel materials and their structural engineering are key for improving the overall efficiency and stability of the semiconductor photocatalysts.[3,4] In terms of suitable catalysts, tantalates were found to exhibit high activity toward photocatalytic hydrogen production.[5−11] In particular, sodium tantalum oxide ($NaTaO_3$) attracted vast attention as one of the most active photocatalysts under UV irradiation.[12] Several parameters that can be engineered affect the efficiency of a photocatalyst such as its morphology, type of crystal structure, heterojunctions, band gap, surface area, porosity, particle size, and decoration of cocatalyst.[13] In general, it is believed that a high degree of crystallinity promotes the activity of a photocatalyst since it reduces the amount of defects and recombination sites for photogenerated electron−hole pairs. Furthermore, the small particle size of nanomaterials is beneficial for charge carrier transport due to the fact that the shorter diffusion path to the surface decreases the possibility of recombination of electron−hole pairs, thus resulting in a higher efficiency. For a number of semiconductor composites, the presence of more than one crystal structure or amorphous and crystalline domains in one sample creates heterojunctions that influence the band gap and charge separation of the photocatalyst as well as increases the efficiency and activity.[14−17] To engineer the structure of sodium tantalates, several synthetic approaches have been reported, for example, solid−solid state reaction,[18−20] sol−gel process,[8,21] hydrothermal synthesis,[22,23] polymerized complex method,[24] soft templating,[25,26] or nanocasting.[27] Among these synthetic methodologies, the hydrothermal route has gained considerable attention since highly crystalline surfactant free nanocrystals could be straightforwardly produced.

Recently, we reported a hydrothermal synthesis of morphology-controlled amorphous and crystalline sodium tantalates starting from sodium tantalum(V) isopropoxide mixed with an isopropanol/ammonium hydroxide solution for overall water splitting.[28] The highest activity toward overall water splitting was achieved with $Na_2Ta_2O_6$ consisting of nanoparticles embedded in an amorphous, porous matrix. Our group also demonstrated a hydrothermal synthesis for the preparation of nanostructured sodium tantalates with different crystal structures.[23] By mixing tantalum(V) ethoxide with aqueous sodium hydroxide solution and subsequent hydrothermal treatment, control over the crystal phase formation was realized giving samples of pure perovskite ($NaTaO_3$), pure pyrochlore ($Na_2Ta_2O_6$), and several samples with perovskite−

Received: July 30, 2015
Accepted: October 6, 2015
Published: October 6, 2015





DOI: 10.1021/acsami.5b06965
ACS Appl. Mater. Interfaces 2015, 7, 23153−23162

pyrochlore mixed phases. The pH of the starting solution controlled the type of crystal structure as well as the morphology of the fabricated catalyst. Under these conditions, perovskite $NaTaO_3$ formed micrometer sized cubic particles, while pyrochlore $Na_2Ta_2O_6$ formed nanometer-sized particles. Photocatalytic investigation for hydrogen production indicated enhanced activity of the nanostructured $NaTaO_3$–$Na_2Ta_2O_6$ sample over pure phase samples with comparable textural parameters, although the highest activity for photocatalytic hydrogen production was found for crystalline $Na_2Ta_2O_6$ nanoparticles with the highest surface area.

Here, we present a series of sodium tantalate samples with different crystalline phases, morphology, surface area, and particle size by using a new hydrothermal method. As starting material, a mixture of tantalum(V) and sodium ethoxide in ethanol was used that produced an amorphous material. The addition of ammonium hydroxide ($NH_4OH$) solution as mineralizer strongly influenced the textural parameters, morphology, and crystalline phases of the obtained materials. Besides the amorphous phase, a range of samples with mixed phases of amorphous–perovskite and perovskite–pyrochlore were synthesized as well as pure pyrochlore $Na_2Ta_2O_6$. Remarkably, all of the crystalline phases were formed as nanoparticles, which was not possible to obtain with previous methodologies. The crystallinity, morphology, and textural parameters of the samples were carefully investigated using X-ray diffraction analysis (XRD), transmission electron microscopy (TEM), and $N_2$ physisorption. Diffuse reflectance was measured with ultraviolet–visible light spectroscopy (UV–vis) to determine the band gap. Finally, the samples were tested as photocatalysts for hydrogen production, and all of the samples demonstrated superior activity over conventional $NaTaO_3$ prepared via solid–solid state reaction route (SS-$NaTaO_3$, used as reference material). Photocatalytic data indicated that samples with a high surface area that contain amorphous phases exhibit much higher hydrogen production rates than pure crystalline samples, showing that a higher degree of crystallinity is not necessary to get higher hydrogen production rates.

## EXPERIMENTAL SECTION

Tantalum(V) ethoxide ($Ta(OEt)_5$, 99.98% trace metals basis), sodium ethoxide (Na(OEt), technical grade ≥95%), and tantalum(V) oxide ($Ta_2O_5$< 5 μm, 99.99%) were purchased from Sigma-Aldrich as well as ammonium hydroxide solution (ACS reagent, 28.0–30.0% $NH_3$ basis). $Na_2CO_3$ (99.8%) was obtained from Acros Organics. All chemicals were used as-received without further purification.

**Synthesis of Sodium Tantalates via Hydrothermal Route.** Sodium tantalum oxide samples were prepared via hydrothermal synthesis by treating an ethanolic solution of tantalum(V) ethoxide and sodium ethoxide mixed with changing amounts of ammonium hydroxide solution for 16 h at 200 °C. In a typical reaction, a solution of tantalum(V) ethoxide (1.6 mmol, 416 μL) dispersed in 2 mL of ethanol and a solution of sodium ethoxide (1.6 mmol, 108 mg) dissolved in 2 mL of ethanol were prepared. They were added simultaneously to an ethanol/$NH_4OH$ solution mixture (46 mL) under strong stirring. By varying the amount of $NH_4OH$ solution (0, 0.25, 1.6, 3.2, 4.0, 4.8, and 9.6 mL), the amount of ethanol was adjusted accordingly (46.0, 45.75, 44.4, 42.8, 42.0, 41.2, and 36.4 mL). The final mixture containing tantalum and sodium ethoxide, $NH_4OH$ solution, and ethanol was stirred for 10 min and then transferred into a 50 mL Teflon lining that was sitting in a 100 mL stainless steel autoclave equipped with temperature and pressure sensors. The autoclave was kept in a heating mantle at 200 °C for 16 h. After it was cooled down to room temperature, the sample was centrifuged and washed three times with deionized water. Subsequently, the white solid product was dried at 90 °C overnight. The sodium tantalate samples were named according to the volume of ammonium hydroxide solution (in mL) that was used during the synthesis: 0-NaTa, 0.25-NaTa, 1.6-NaTa, 3.2-NaTa, 4.0-NaTa, 4.8-NaTa, and 9.6-NaTa.

**Preparation of Reference Material SS-$NaTaO_3$.** To serve as a reference material, $NaTaO_3$ was prepared via solid–solid state synthesis[12,23] and was designated SS-$NaTaO_3$. A solid mixture of $Ta_2O_5$ (0.442 g) and $Na_2CO_3$ (0.113 g, 5% excess) was ground thoroughly, and the powder was calcined at 900 °C for 1 h (with a ramping rate of 5 °C/min), then cooled down to room temperature and ground again. Subsequently, the material was calcined at 1150 °C for 10 h with a ramping of 5 °C/min. Excess sodium was washed out with water after the calcination.

**Characterization.** TEM images were obtained with an H-7100 electron microscope (100 kV) from Hitachi. High-resolution TEM (HR-TEM) images of samples were obtained with an HF-2000 microscope (Hitachi) equipped with a cold field emission gun. The acceleration voltage was 200 kV. Samples were prepared on carbon film covered grids. Nitrogen adsorption isotherms of samples were measured with an ASAP 2010 adsorption analyzer (Micrometrics) at 77 K. Prior to the measurements, the samples were degassed at 120 °C for 12 h. Total pore volumes were determined using the adsorbed volume at 0.97 $p/p_0$. The BET (Brunauer–Emmett–Teller) surface area was determined from the relative pressure range between 0.06 and 0.2. XRD patterns were collected at room temperature on a Stoe theta/theta diffractometer in Bragg–Brentano geometry (Cu K$\alpha$1/2 radiation). The measured patterns were evaluated qualitatively by comparison with entries from the ICDD-PDF-2 powder pattern database. Scherrer equation and integral breadth were calculated using the Size/Strain module of the Win XPOW 3.04 software from STOE, correcting the data with an internal Si standard. Peak fitting was performed using the Pattern Fitting module of Win XPOW 3.04. UV–vis was conducted in diffuse reflectance mode on a Varian Cary 5G with praying mantis setup using MgO as white standard.

**Photocatalytic Test.** Photocatalytic $H_2$ production was conducted with an in-house built inner irradiation photoreactor cell with a total volume of 260 mL. For water splitting with sacrificial agent, the reactor was filled with 200 mL of 10 vol % methanol in deionized water. Overall water splitting was conducted in 200 mL of MQ water. One-hundred milligrams of solid catalyst was dispersed in 10 mL of reactor solution by sonicating for 20 min prior to addition into the reactor. The solution inside the photoreactor was stirred during the catalytic test. A 150 W middle pressure mercury lamp (TQ 150) from Peschl Ultraviolet was used as the light source, and irradiation was performed in 1- or 2-h intervals. An Ar flow of 50 mL $min^{-1}$ was connected to the reactor and purged through the solution, carrying the evolved gases out of the reactor via another connection into a gas analyzer (X-STREAM Enhanced XEGP Gas Analyzer from Emerson) equipped with a detector for carbon dioxide (infrared detector), oxygen (paramagnetic detector), and hydrogen (heat conductivity detector). For the overall water splitting measurement, the samples were irradiated for 5 h until only hydrogen and oxygen signals were achieved; then the light was switched off and the reactor setup purged with argon to remove all traces of hydrogen and oxygen. Subsequently, the lamp was switched on, and hydrogen and oxygen evolution rates were measured.

The activity of the photocatalysts was evaluated by calculating the apparent photocatalyst activity (APA) using the following equation:[29]

$$\mathrm{APA} = \frac{\text{moles of } H_2 \text{ evolution } (\mu\text{mol})}{X \cdot Y \cdot Z \cdot W} \quad (1)$$

Where $X$ = weight of catalyst (g), $Y$ = volume of reactant (L), $Z$ = duration of reaction (h), and $W$ = power of lamp (W). Using APA to evaluate photocatalyst activity facilitates comparison of the performance of materials in different reactor designs and is also suitable for comparison of photocatalysts that are tested under the same reaction conditions.[29] Since the catalysts of this series were tested under equal conditions (same light source, reactor, catalyst concentration, and argon flow), it is feasible to apply this equation for evaluating the activity of the catalysts.


DOI: 10.1021/acsami.5b06965
ACS Appl. Mater. Interfaces 2015, 7, 23153–23162

## RESULTS AND DISCUSSION

Sodium tantalates featuring different morphologies, surface areas, and particle sizes were synthesized herein via a convenient hydrothermal treatment (16 h at 200 °C) of tantalum(V) and sodium ethoxide in ethanol solution, which was controlled through the addition of specific amounts of $NH_4OH$ solution. The crystal structures of the prepared composites were analyzed using XRD, and the respective crystalline domain size was calculated using the Scherrer equation. As seen in Figure 1, the sample without addition of

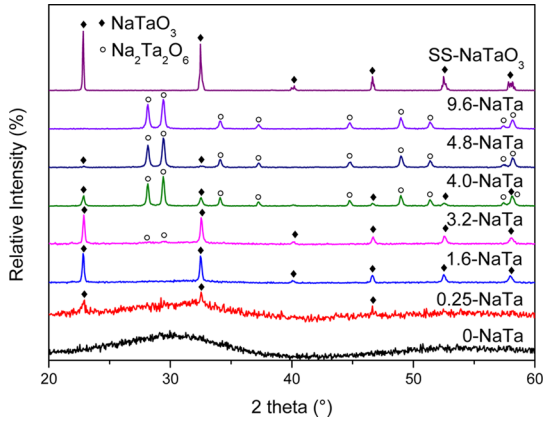


**Figure 1.** Wide angle XRD patterns of sodium tantalates prepared via hydrothermal synthesis by varying the amount of ammonium hydroxide solution (volume in mL denoted by the number in each sample label) and reference material SS-$NaTaO_3$.

$NH_4OH$ solution (0-NaTa) exhibited an amorphous structure, whereas the addition of $NH_4OH$ led to the formation of crystalline domains. The lowest content of ammonium hydroxide solution (0.25 mL, the sample is labeled as 0.25-NaTa) shows the typical broad signals that are indicative of an amorphous phase with characteristic perovskite $NaTaO_3$ reflexes (JCPDS No.:74−2479). Increasing the $NH_4OH$ solution content to 1.6 mL during the synthesis (1.6-NaTa) increased the crystallinity of the $NaTaO_3$ phase. When the $NH_4OH$ solution amount was further increased to 3.2 mL (3.2-NaTa), the XRD pattern showed that the sample consisted of a $NaTaO_3$−$Na_2Ta_2O_6$ mixture with very pronounced $NaTaO_3$ reflections and very small $Na_2Ta_2O_6$ signals (JCPDS No.: 70−1155). The portion of the $Na_2Ta_2O_6$ phase was increased by using 4.0 mL of $NH_4OH$ solution (4.0-NaTa), yielding a highly crystalline perovskite−pyrochlore sodium tantalate composite. Further increasing the $NH_4OH$ amount to 4.8 mL (4.8-NaTa) changed the ratio of the crystalline phases to favor the pyrochlore $Na_2Ta_2O_6$, while the reflections corresponding to $NaTaO_3$ were strongly diminished. Finally, the addition of 9.6 mL of $NH_4OH$ solution (9.6-NaTa), which is the highest amount of $NH_4OH$ used in this series, produced a pure $Na_2Ta_2O_6$ phase. The reference SS-$NaTaO_3$ sample produced by solid−solid state reaction shows sharp crystalline reflections as expected. From the XRD analysis, the size of the crystalline domains was estimated using the Scherrer equation:[30,31]

$$\tau = \frac{K\lambda}{\beta \cos(\theta)} \quad (2)$$

with $\tau$ = size of the crystalline domain, $K$ = form factor,[31] $\lambda$ = X-ray wavelength, $\beta$ = integral breadth,[32] and $\theta$ = Bragg angle. The crystalline domain size was estimated by the Scherrer equation for all samples of the series, apart from 0-NaTa and 0.25-NaTa, which showed no or little crystalline diffraction peaks in their XRD pattern. For the samples 1.6-NaTa, 3.2-NaTa, and 4.0-NaTa, the crystallite sizes of $NaTaO_3$ were calculated to be about 69, 61, and 43 nm, respectively. The pyrochlore $Na_2Ta_2O_6$ that was detected in the 4.0-NaTa, 4.8-NaTa, and 9.6-NaTa samples exhibited an average crystallite size of 73, 55, and 49 nm, respectively. The particle size of SS-$NaTaO_3$ was determined by TEM analysis to be about 3−6 $\mu$m (Figure S1).

The shape and morphology of materials can play a critical role in their catalytic performance. To investigate the morphology of the samples, the samples were investigated with TEM, and the images are presented in Figure 2. The analysis showed a porous network-like structure for amorphous 0-NaTa. The 0.25-NaTa sample consists of amorphous network structure and small fraction of nanocrystals with an average particle size of 85 nm. The fraction of crystalline $NaTaO_3$ nanoparticles compared to the amorphous network increased for 1.6-NaTa, where XRD analysis showed mainly crystalline

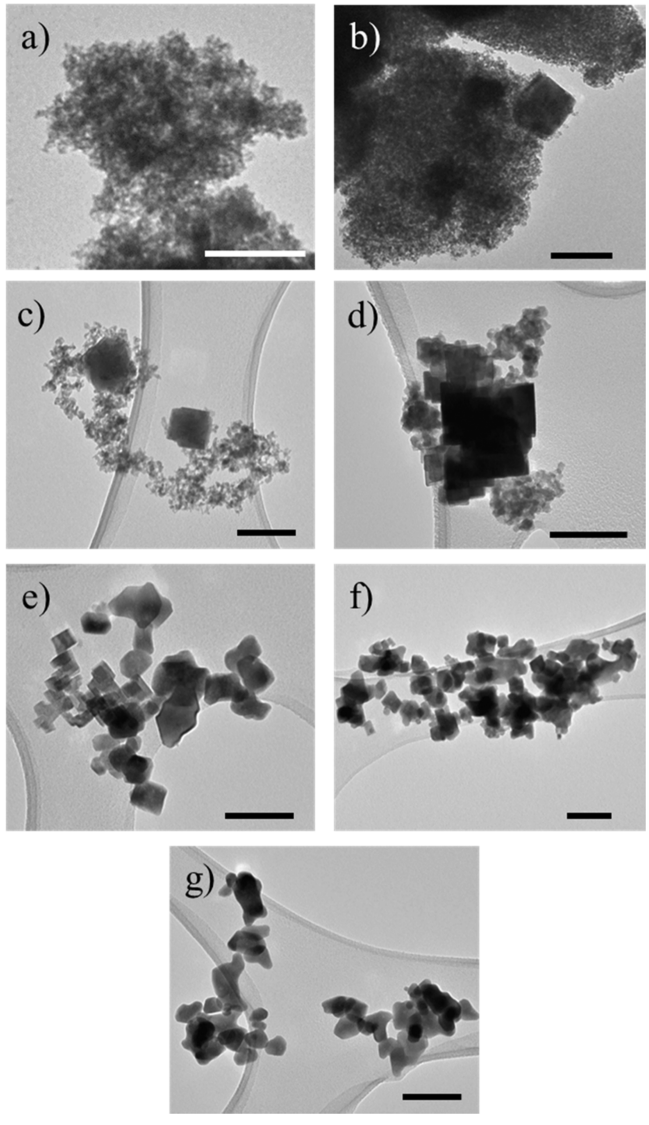


**Figure 2.** TEM images of (a) 0-NaTa, (b) 0.25-NaTa, (c) 1.6-NaTa, (d) 3.2-NaTa, (e) 4.0-NaTa, (f) 4.8-NaTa, and (g) 9.6-NaTa. All scale bars are 100 nm.


DOI: 10.1021/acsami.5b06965
ACS Appl. Mater. Interfaces 2015, 7, 23153−23162

$NaTaO_3$ phase. Since the amorphous structure gives low signals in XRD compared to crystalline structures, the sample appeared to be crystalline according to the pattern. Similar observations were made for 3.2-NaTa. The image mainly depicts nanoparticles set in an amorphous network, although the quantity of amorphous matrix decreased compared to the 1.6-NaTa sample. The average particle sizes found by TEM analysis for 1.6-NaTa and 3.2-NaTa samples were around 75 and 64 nm, which are lower than the particle size of 0.25-NaTa. These values fit well to the crystalline domain size determined by the Scherrer eq (69 and 61 nm, respectively). With increasing $NH_4OH$ amount, the amorphous structure was no longer observed for 4.0-NaTa, which showed a crystalline composite of $NaTaO_3$–$Na_2Ta_2O_6$ mixed phases, as confirmed by XRD analysis. For this sample, the particle size was determined by TEM analysis to be about 66 nm on average. However, with regard to particle morphology, particles with a cubic morphology showed an average size of 53 nm, which match the crystallite size determined by Scherrer equation for the $NaTaO_3$ phase (43 nm). Particles with a rounded and more undefined shape were found to be about 79 nm in size by TEM analysis. These values match the crystalline domain size determined by the Scherrer equation for the $Na_2Ta_2O_6$ phase (73 nm). For the samples 4.8-NaTa and 9.6-NaTa, the $NaTaO_3$ phase diminished from the XRD patterns, while the $Na_2Ta_2O_6$ phase became more distinct. TEM images of these samples depict nanoparticles with predominantly smooth rounded shapes; thus, the rounded particle morphology was assigned to be $Na_2Ta_2O_6$. The average sizes of these rounded particles were determined by TEM analysis to be 62 and 51 nm for 4.8-NaTa and 9.6-NaTa, respectively, which is in agreement with the crystalline domain size calculated by the Scherrer eq (55 and 49 nm, respectively). The TEM survey showed that the morphology and particle shape are altered by using different amounts of $NH_4OH$ solution. For comparison, a TEM image of the reference sample SS-$NaTaO_3$ is shown in Figure S1 where randomly shaped, dense particles are observed.

Composites of amorphous and crystalline samples or mixtures of different crystalline phases have proven to enhance the photocatalytic activity of samples toward water splitting.[28,33] Therefore, two samples (0.25-NaTa and 4.0-NaTa) with mixed morphologies and phases were investigated in detail by HR-TEM. First, 0.25-NaTa was examined as it is a mixture of amorphous sodium tantalate and crystalline $NaTaO_3$ nanoparticles (Figure 3a,b). As shown in Figure 3, panel a, a nanoparticle is reaching out of a larger domain, which was later identified as the amorphous matrix. In high resolution, the nanoparticle shows ordered atomic structure as seen in Figure 3, panel b, whereas the amorphous matrix shows no ordering on the atomic level, hence the amorphous structure. As shown before by XRD analysis, 0.25-NaTa contains crystalline $NaTaO_3$; therefore, the crystalline nanoparticles are assumed to be $NaTaO_3$. The second sample, 4.0-NaTa, was examined by HR-TEM to observe the composite of the two crystalline phases of sodium tantalate, namely perovskite $NaTaO_3$ and pyrochlore $Na_2Ta_2O_6$. The image in Figure 3, panel c shows a group of nanoparticles with different morphologies of smooth and sharp-edged surfaces. As highlighted in Figure 3, panel d, the round-shaped particle has a lattice constant of 0.30 nm, while the cubic particle has 0.39 nm spacing between the atomic layers, which can be assigned to the *d*-spacing of the {222} facets of $Na_2Ta_2O_6$ and the {100} or {001} facets of $NaTaO_3$, respectively.[34] The {hkl} values were taken from the

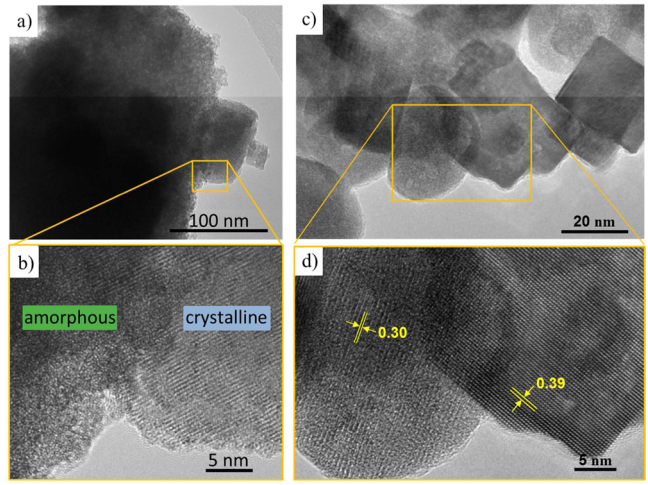


**Figure 3.** (a) TEM and (b) HR-TEM images of the composite sample 0.25-NaTa, consisting of $NaTaO_3$ nanoparticles and an amorphous sodium tantalate matrix. (c) TEM and (d) HR-TEM images of 4.0-NaTa that consists of perovskite and pyrochlore crystal structure.

JCPDS data files. This HR-TEM examination shows the presence of two different particle morphologies along with the two crystal structures, namely $NaTaO_3$ and $Na_2Ta_2O_6$, in the composite sample of 4.0-NaTa.

Since the composition of the samples with perovskite ($NaTaO_3$) and pyrochlore ($Na_2Ta_2O_6$) sodium tantalate phases is clear in terms of the Ta/Na ratio, the composition of the amorphous samples was further examined by energy-dispersive X-ray spectroscopy (EDX) and X-ray photoelectron spectroscopy (XPS) measurements, which describe the bulk composition of a sample or surface composition, respectively. As determined by EDX analysis (spectra not shown), 0-NaTa has a Ta/Na ratio of 2.2, and 0.25-NaTa has a Ta/Na ratio of 1.8. The composition of both samples is fairly similar to a Ta/Na ratio of about 2 for bulk analysis. For the surface composition analysis, XPS analysis showed that 0-NaTa and 0.25-NaTa samples have Ta/Na ratios of 1.3 and 1.2, respectively. These results indicate a formation of sodium tantalate with a Ta/Na ratio of approximately 1 on the surface of the amorphous samples, which is similar to the composition of the crystalline phases. Additionally, the oxidation states of tantalum and sodium were determined by XPS analysis for the amorphous samples to define the phase of tantalate. As shown in Figure S2a, the binding energies for 0-NaTa are located at 27.7 and 25.9 eV for Ta $4f_{5/2}$ and $4f_{7/2}$, respectively. For 0.25-NaTa, the binding energies for Ta $4f_{5/2}$ and $4f_{7/2}$ are at slightly lower energies at 27.6 and 25.7 eV, respectively. The peak of Na(I) (Figure S2b) is positioned at 1071.2 and 1071.1 eV for 0-NaTa and 0.25-NaTa, respectively. These values for Ta 4f and Na 1s binding energies are in agreement with previously reported values for $NaTaO_3$.[28,35] Thus, although the samples are highly amorphous, 0-NaTa and 0.25-NaTa have a surface composition similar to that of $NaTaO_3$.

The specific surface area of a material is a crucial feature for its catalytic activity. Therefore, $N_2$-physisorption was performed to determine the surface area of the sodium tantalates, and the results are presented in Table 1. Amorphous 0-NaTa had a surface area of 200 $m^2\ g^{-1}$. When 0.25 mL of $NH_4OH$ solution was used during the synthesis, the sample (0.25-NaTa) had a surface area of 236 $m^2\ g^{-1}$. Increasing the amount of $NH_4OH$ solution led to a decrease in surface area due to the loss of the


DOI: 10.1021/acsami.5b06965
ACS Appl. Mater. Interfaces 2015, 7, 23153−23162

**Table 1. Amount of Ammonium Hydroxide Solution, Surface Areas, Band Gap Energies, Hydrogen Production Rates after 2 h from Water Splitting Using Methanol as Sacrificial Agent**

| sample | $NH_4OH$ solution (mL) | $S_{BET}$ ($m^2$ $g^{-1}$) | band gap energy (eV) | $H_2$ rate (mmol $h^{-1}$) | APA[a] ($\mu$mol $g^{-1}$ $L^{-1}$ $h^{-1}$ $W^{1-}$) |
|---|---|---|---|---|---|
| 0-NaTa | 0.00 | 200 | 4.4 (amorphous) | 2.4 | 800 |
| 0.25-NaTa | 0.25 | 236 | 4.6 (amorphous) + 4.1 ($NaTaO_3$) | 3.6 | 1200 |
| 1.6-NaTa | 1.60 | 83 | 4.6 (amorphous) + 4.1 ($NaTaO_3$) | 3.0 | 1000 |
| 3.2-NaTa | 3.20 | 54 | 4.6 (amorphous) + 4.1 ($NaTaO_3$) | 1.5 | 500 |
| 4.0-NaTa | 4.00 | 26 | 4.1 ($NaTaO_3$) + 4.8 ($Na_2Ta_2O_6$) | 1.4 | 470 |
| 4.8-NaTa | 4.80 | 26 | 4.0 ($NaTaO_3$) + 4.9 ($Na_2Ta_2O_6$) | 1.1 | 370 |
| 9.6-NaTa | 9.60 | 29 | 4.8 ($Na_2Ta_2O_6$) | 1.0 | 330 |
| SS-$NaTaO_3$ | – | 2 | 4.0 ($NaTaO_3$) | 0.8 | 270 |

[a]Apparent photocatalytic activity (APA) calculated according to eq 1.

amorphous porous network and formation of larger crystalline particles. The value dropped dramatically from 236 $m^2$ $g^{-1}$ for 0.25-NaTa to 83 $m^2$ $g^{-1}$ for 1.6-NaTa, and further to 54 and 26 $m^2$ $g^{-1}$ for 3.2-NaTa and 4.0-NaTa, respectively. The amount of amorphous structure decreased in this order, up to sample 4.0-NaTa, which was characterized as highly crystalline by XRD and TEM. Further increasing the $NH_4OH$ had a negligible effect on the surface areas of 4.8-NaTa and 9.6-NaTa. The surface area of the reference SS-$NaTaO_3$ material was determined to be 2 $m^2$ $g^{-1}$. The decrease in surface area with increasing $NH_4OH$ usage correlates with the decrease in amorphous structure and increasing degrees of crystallinity along the series. Similar values of surface area for 4.0-NaTa, 4.8-NaTa, and 9.6-NaTa match with the observations that the last three samples did not possess an amorphous matrix as shown by XRD and TEM analysis.

It should be mentioned that the morphology and crystal phases of the obtained materials are highly dependent on the pressure of the autoclaves. Thus, the pressure of the autoclave reactor was monitored, and by doing so, we could straightforwardly reproduce the synthesis. Varying the amount of $NH_4OH$ in the starting solution alters the composition of the reaction mixture. While heating under hydrothermal conditions at a constant temperature of 200 °C, the pressure inside the reactor was monitored throughout the synthesis. As shown in Figure S3, the pressure changes according to the amount of added $NH_4OH$. Without any $NH_4OH$ in the starting solution, the hydrothermal reactor reached a pressure of 18.3 bar that produced amorphous sodium tantalate. The addition of 0.25 mL of $NH_4OH$ solution gave an average pressure of 18.4 bar, similar to the pressure when no $NH_4OH$ was added. Although the pressure did not change substantially, the sample contained crystalline particles of $NaTaO_3$. Clearly, the mineralizer is responsible for the formation of crystalline domains at small pressure differences, though a high pressure might enhance crystallization. Increasing the amount of $NH_4OH$ consequently increased the pressure as well. Pressures of 18.8, 20.0, and 20.5 bar were measured for 1.6-NaTa, 3.2-NaTa, and 4.0-NaTa, respectively. As it is mentioned earlier, 4.0-NaTa is highly crystalline, while samples with lower $NH_4OH$ addition partly possessed amorphous structures. Likewise, samples that reached higher reaction pressures during the synthesis obtained a highly crystalline structure. The pressure level inside the reactor was dependent on the temperature and composition of the reaction solution as it rose with the amount of $NH_4OH$, which influences crystallization and phase formation of the samples. To exclude the possibility that pressure alone is the driving force for crystallization, a synthesis without the addition of mineralizer was carried out at a pressure of 90 bar. The autoclave was heated to 200 °C for 16 h, and the white product was analyzed by XRD analysis that showed amorphous material (Figure S4). This experiment underlines the necessity of the mineralizer for the crystal formation.

To ascertain if a semiconductor can be used as a photocatalyst and at which energy of light it can be excited, the band gap between the valence and conduction bands of the semiconductor is determined using UV–vis spectroscopy. The band gap energy of the sodium tantalate samples was defined via Tauc plots that are shown in Figure 4. For clarity, Figure 4, panel a shows the Tauc plots of samples that contained amorphous phase, and Figure 4, panel b compiles the crystalline samples; the reference material SS-$NaTaO_3$ is shown in both figures. The diffuse reflectances (Figure S5) were transferred via

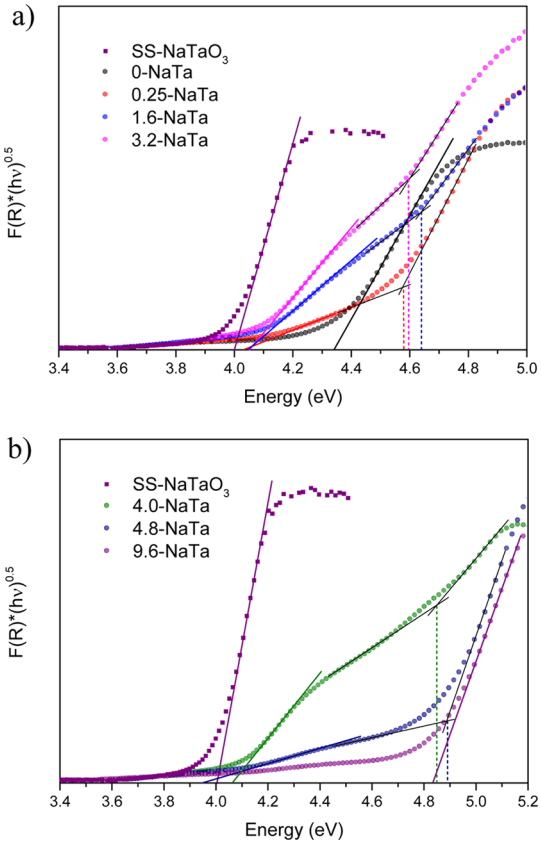


**Figure 4.** Tauc plots of (a) 0-NaTa, 0.25-NaTa, 1.6-NaTa, 3.2-NaTa, and (b) 4.0-NaTa, 4.8-NaTa, 9.6-NaTa; the Tauc plot of reference sample SS-$NaTaO_3$ is shown in both graphs. For clarity, the data of SS-$NaTaO_3$ are omitted above 4.5 eV.


DOI: 10.1021/acsami.5b06965
ACS Appl. Mater. Interfaces 2015, 7, 23153–23162

Kubelka–Munk function into Tauc plots where tantalates are considered as indirect semiconductors.[36] The band gap energy values are summarized in Table 1. As seen from the graph, SS-$NaTaO_3$ has a band gap of 4.0 eV, which is characteristic for perovskite sodium tantalate.[27,37] The band gap of amorphous 0-NaTa was 4.4 eV and is in good agreement with reported values.[38] The 0.25-NaTa exhibits two energy gaps of 4.6 and 4.1 eV, which are linked to the amorphous phase in the sample (4.4 eV, as shown for 0-NaTa) and the minor fraction of crystalline $NaTaO_3$, respectively. The next samples 1.6-NaTa and 3.2-NaTa also had two band gaps because they both possessed amorphous and partly crystalline structures. For both samples, the crystalline $NaTaO_3$ part exhibits a band gap of 4.1 eV, while the amorphous phase has a band gap of 4.6. As a remark, 3.2-NaTa also contained $Na_2Ta_2O_6$ according to XRD analysis; nonetheless, this phase was not observed in Tauc plot since the amount is very low based on the small reflections in the XRD pattern. Continuing with 4.0-NaTa, the sample shows two band gaps of 4.1 and 4.8 eV that were assigned to $NaTaO_3$ and $Na_2Ta_2O_6$ phases, respectively. This value is in the range of reported values for $Na_2Ta_2O_6$ (4.6 eV).[39] For 4.8-NaTa, a similar behavior was observed. A small slope in the Tauc plot indicated a band gap of 4.0 eV and another one of 4.9 eV that were assigned to $NaTaO_3$ and the dominating $Na_2Ta_2O_6$ phase, respectively. The band gap value of 4.8 eV for $Na_2Ta_2O_6$ phase was also observed for 9.6-NaTa. The study of the band gap energies showed that SS-$NaTaO_3$ had a band gap of 4.0 eV analogous to the samples containing $NaTaO_3$ nanoparticles that have an estimated band gap of 4.1 eV.

The activity of the samples toward photocatalytic hydrogen production was evaluated using photocatalytic water splitting with methanol as sacrificial agent in a flow reactor that was connected to a gas analyzer. Water splitting with a sacrificial agent such as methanol is commonly applied to evaluate the activity of photocatalysts for water splitting since overall water splitting is challenging due to the water oxidation half reaction.[40−42] Additionally, the alcohol is irreversibly oxidized, which suppresses the back reaction ($2O_2 + H_2 \rightarrow 2H_2O$) and enriches the electron concentration in the photocatalyst and consequently boosts the hydrogen production rate.[40,43] A generally acknowledged step-by-step reaction of the methanol oxidation includes the following reactions:[44]

$$CH_3OH + 2h^+ \rightarrow HCHO + 2H^+ \quad (3)$$

$$HCHO + H_2O + 2h^+ \rightarrow HCOOH + 2H^+ \quad (4)$$

$$HCOOH + 2h^+ \rightarrow CO_2 + 2H^+ \quad (5)$$

The overall reaction for water splitting with methanol can be written as[44]

$$CH_3OH + H_2O \rightarrow CO_2 + 3H_2 \quad (6)$$

As shown in reaction 6, the hydrogen ions that are produced in the methanol oxidation reaction (reactions 3−5) are reduced by excited electrons to molecular hydrogen.

The hydrogen production rates of the samples for water splitting using methanol as sacrificial agent are shown in Figure 5. All samples were irradiated for 2 h in a 180 mL of $H_2O$/20 mL of methanol solution using 100 mg of catalyst, and the hydrogen rates are presented in Table 1. Because of the reason that the lamp after ignition will reach its maximum performance and stabilize after a certain time, hydrogen generation rates of the samples were compared after 2 h of irradiation. As shown,

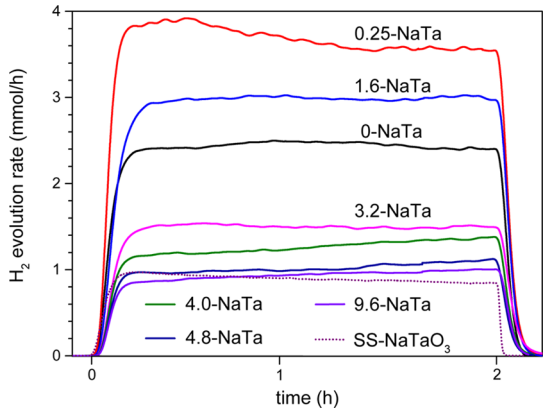


**Figure 5.** Hydrogen production rates of the sample series produced via hydrothermal synthesis and reference material SS-$NaTaO_3$. The 100 mg sample was dispersed in 200 mL (concentration 0.5 g $L^{-1}$) of 10 vol % methanol aqueous solution. A 150 W middle pressure mercury lamp was used as the light source.

amorphous 0-NaTa produced 2.4 mmol $h^{-1}$ hydrogen, which is higher than the highly crystalline reference sample SS-$NaTaO_3$, which had a $H_2$ rate of 0.8 mmol $h^{-1}$. The high surface area of 0-NaTa (200 $m^2$ $g^{-1}$) is clearly responsible for the higher activity, indicating that a network-like amorphous structure can be advantageous over crystallinity. The 0.25-NaTa sample with amorphous network containing small $NaTaO_3$ nanoparticles generated 3.6 mmol $h^{-1}$ hydrogen and was the most active sample of the series. Compared to 0-NaTa, the surface area of 0.25-NaTa is 15% higher (236 $m^2$ $g^{-1}$), though the activity is 50% higher. The increase could be assigned to the mixture of crystalline $NaTaO_3$ nanoparticles and amorphous porous network. In this composite sample, the presence of both phases might increase the charge carrier separation as it is known for heterojunction materials and thus enhance the photocatalytic activity.[33] Similar amorphous–crystalline composite samples have been demonstrated to form heterojunctions and improve separation of photoexcited charges if the thickness of the amorphous region is small.[45−49] In our case, the amorphous matrix can reach distances of several-hundred nanometers; however, as it consists of a porous network, the minimum diffusion path for charge carriers through the amorphous matrix is only a few nanometers, as shown by the HR-TEM observation (Figures 3a,b and S6c,d). We attributed the high photocatalytic activity to the porous nature of the amorphous matrix, which makes the diffusion of charge carriers to the electrolyte interface quite facile.

A higher degree of crystallinity mixed with amorphous structure was observed for 1.6-NaTa. The sample generated 3.0 mmol $h^{-1}$ hydrogen, which is more active than 0-NaTa, although the surface area decreased greatly to 83 $m^2$ $g^{-1}$ for 1.6-NaTa. For 0.25-NaTa and 1.6-NaTa, the ratio between the amorphous and crystalline phases is beneficial for photocatalysis, which can be attributed to the mixture of the amorphous porous network and $NaTaO_3$ nanoparticles resulting in composite samples. However, for 3.2-NaTa, the sample that contained only a minor fraction of amorphous network, the photocatalytic activity decreased to 1.5 mmol $h^{-1}$ hydrogen produced. Similar rates were determined for the highly crystalline samples 4.0-NaTa, 4.8-NaTa, and 9.6-NaTa with 1.4, 1.1, and 1.0 mmol $h^{-1}$ generated hydrogen. Among the nanocrystalline samples with similar surface areas, 4.0-TaNa consisted of an almost equal fraction of pyrochlore and


DOI: 10.1021/acsami.5b06965
ACS Appl. Mater. Interfaces 2015, 7, 23153−23162

perovskite phases as judged by the XRD pattern. This composite sample showed higher photocatalytic performance than pure $Na_2Ta_2O_6$ (9.6-NaTa) due to the presence of both crystalline phases also shown by HR-TEM analysis. It is worth mentioning that all samples of the series showed a higher activity toward photocatalytic hydrogen production than the reference SS-$NaTaO_3$. Furthermore, the higher rates for photocatalytic hydrogen production were achieved by samples that are either amorphous or contain a large quantity of amorphous structure. The most active sample 0.25-NaTa, which contains large quantities of amorphous phase and a small fraction of perovskite $NaTaO_3$, has an apparent photocatalytic activity (APA) of 1200 $\mu$mol $g^{-1}$ $L^{-1}$ $h^{-1}$ $W^{1-}$, which is around 4.5-times higher than highly crystalline SS-$NaTaO_3$. To give an overview of the photocatalytic activity of all samples, the APA values were calculated for all samples and presented in Table 1. The trend of the APA value follows the same behavior of the hydrogen production rate as is expected. Our data confirm that producing active tantalate based photocatalysts does not automatically requires a high degree of the crystallinity of the catalyst or solid state reactions run at a temperature >1000 °C, which is time and energy consuming.

The photocatalytic hydrogen production is connected to the band gap, morphology, surface area, and crystallinity of the samples, which was earlier attributed to the amount of $NH_4OH$ that was added during the hydrothermal synthesis. The BET surface area, $H_2$ production rate, and the crystal phase of the materials have been summarized in a graph in Figure 6. The

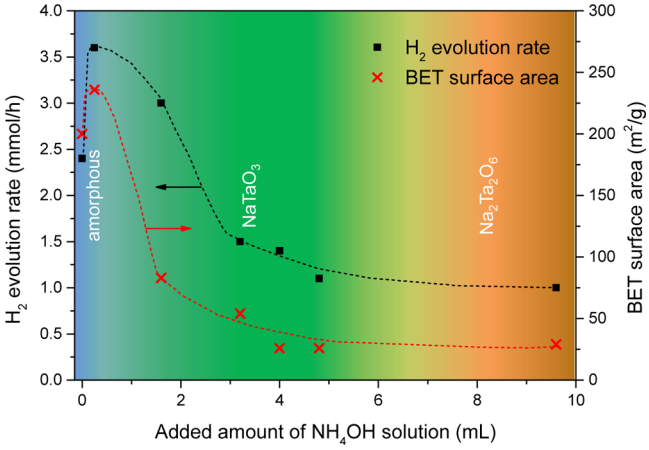


**Figure 6.** Hydrogen evolution rate (left *y*-axis) and BET surface area (right *y*-axis) displayed over amount of ammonium hydroxide solution added to the synthesis. Furthermore, the amorphous and crystalline phases are indicated for the applied amount of $NH_4OH$ solution.

hydrogen rate and BET surface area are depicted over the amount of $NH_4OH$ used in the solution, and the color in the back of the graph indicates the three phases of sodium tantalate that were obtained either separately or together. The starting point of the curve is made by the amorphous sample 0-NaTa with a hydrogen production rate of 2.4 mmol $h^{-1}$ and a surface area of 200 $m^2$ $g^{-1}$. Addition of a small amount of $NH_4OH$ (0.25 mL) to the starting solution initiated crystallization of $NaTaO_3$ and increased the hydrogen rate as seen in the graph to the maximum of 3.6 mmol $h^{-1}$. This sample also obtained the highest surface area of 236 $m^2$ $g^{-1}$ since it possessed an amorphous network with only a small fraction of crystalline particles, which positively influenced the activity of the sample. This effect can be seen more clearly for 1.6-NaTa. The sample has a substantially lower surface area than 0-NaTa but shows higher activity toward hydrogen production due to the presence of nanoparticles in the amorphous network. Further addition of $NH_4OH$ solution decreased the amount of amorphous phase and surface areas, and the higher degrees of crystallinity did not improve the photocatalytic activity.

Stability toward oxidation and passivation is a crucial factor in photocatalysis. To investigate the long-term photocatalytic stability, the most active sample 0.25-NaTa was irradiated over 48 h. As seen in Figure S6a, the sample generated hydrogen at an initial rate of 3.9 mmol $h^{-1}$ and stabilized after 5 h at a rate of 3.0 mmol $h^{-1}$. After 2 h, the sample generated 3.6 mmol $h^{-1}$ of hydrogen, as it was shown for 0.25-NaTa in Figure 5 before, which indicates a good reproducibility of the experiment and photocatalytic activity of the catalyst. This deactivation or lowered hydrogen production over time was also observed in SS-$NaTaO_3$ as shown in Figure 5. After 48 h of hydrogen generation, the sample was characterized by XRD, TEM, $N_2$-physisorption, EDX, and HR-TEM to determine if the structure and morphology of the sample were altered during catalysis. As shown in Figure S6b, the diffraction pattern of 0.25-NaTa after 48 h in the photocatalytic reactor is very similar to the pattern of the as-made 0.25-NaTa. In addition, there was no significant change in morphology observed by TEM analysis. Images of 0.25-NaTa after 48 h of hydrogen evolution are presented in Figure S6c,d. The amorphous matrix, which surrounds the nanoparticles, showed similar morphology of a porous network as for as-made 0.25-NaTa. The $NaTaO_3$ nanoparticles however show parts of amorphous structure on the outer layer of the crystalline structure, as highlighted in Figure S6d. This suggests that the crystalline nanoparticles partly corrode during photocatalytic hydrogen production and lose the crystalline structure to some extent. This phenomenon might be related to the diminished sodium amount of the sample, which was washed out during the catalytic reaction, as well as the decay of photocatalytic activity in the first 5 h. To examine the composition of 0.25-NaTa after 48 h of hydrogen production, the sample was studied by EDX analysis (spectra not shown). In comparison to as-made 0.25-NaTa, the amount of sodium was strongly reduced in the sample. The as-made 0.25-NaTa had a Ta/Na ratio of 1.8 as determined by EDX, and after 48 h in the photoreactor, the sample showed a Ta/Na ratio of 10.2, meaning the amount of sodium was reduced by a factor of 5.5. The sodium was predominantly washed out of the amorphous structure during the reaction, as the $NaTaO_3$ phase of the nanoparticles was observed by XRD analysis after the catalytic reaction. The slight deactivation of the material can be attributed to the loss of sodium in the first 5 h of the reaction. To further evaluate a possible change in morphology, the BET surface area was determined after the stability test. A decrease of 10% in surface area was measured after 48 h of hydrogen production. These results suggest that the material shows overall decent long-term stability, although the hydrogen production rate decays in the first hours until it stabilizes. A higher stability might be achieved with the application of cocatalysts;[50] however, this was not part of this study.

Since 0.25-NaTa showed the highest activity toward photocatalytic hydrogen production from a water/methanol solution, the sample was further tested for overall water splitting. Overall water splitting is genuinely the desired photocatalytic reaction for producing clean hydrogen (and oxygen in a stoichiometric ratio of 2:1) without the formation


DOI: 10.1021/acsami.5b06965
ACS Appl. Mater. Interfaces 2015, 7, 23153−23162

of carbon dioxide from oxidation of the sacrificial agent (e.g., methanol). The reaction is more challenging due to a four electron transfer and the formation of oxygen bonds:[51]

$$2H^+ + 2e^- \rightarrow H_2 \quad E^\circ = 0\ V\ vs\ RHE \tag{7}$$

$$2H_2O \rightarrow O_2 + 4H^+ + 4e^- \quad E^\circ = 1.23\ V\ vs\ RHE \tag{8}$$

$$2H_2O \rightarrow 2H_2 + O_2 \quad \Delta G^\circ = 237.2\ kJ\ mol^{-1} \tag{9}$$

Since the oxidation potential of water has higher energy than the oxidation potential of methanol,[41,42] the hydrogen production rate is lower for overall water splitting. To investigate the ability of photocatalysts for overall water splitting without any cocatalyst decoration, the most active sodium tantalate sample (0.25-NaTa) and reference SS-$NaTaO_3$ sample were tested. The hydrogen and oxygen evolution rates are shown in Figure 7. As illustrated, $H_2$ and

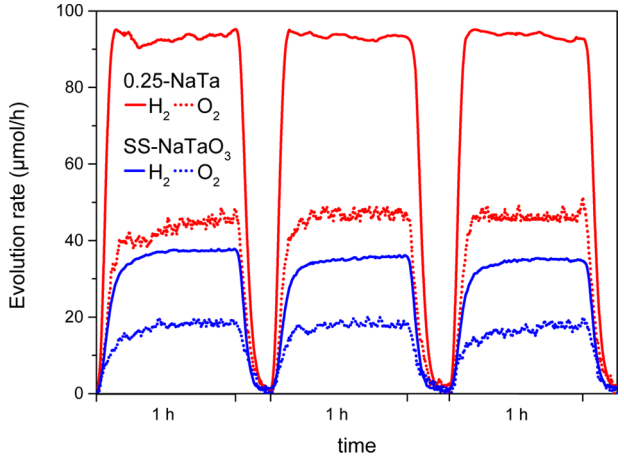


**Figure 7.** Photocatalytic overall water splitting performed with 0.25-NaTa and reference material SS-$NaTaO_3$. A 100 mg sample was dispersed in 200 mL (concentration 0.5 g $L^{-1}$) of MQ water. A 150 W middle pressure mercury lamp was used as the light source.

$O_2$ were produced in a stoichiometric ratio of approximately 2:1. The catalysts were tested in three runs over 1 h each. Over the total 3 h, the samples showed no deactivation. The hydrogen production rate of 0.25-NaTa and SS-NaTaO3 was 94 $\mu$mol $h^{-1}$ and 35 $\mu$mol $h^{-1}$, respectively. Amorphous/partly crystalline 0.25-NaTa showed a ~3-fold better catalytic activity than SS-$NaTaO_3$, although the reference is highly crystalline. Despite a low number of defects and electron−hole recombination sites in a crystalline structure, SS-$NaTaO_3$ has a low surface area of 2 $m^2$ $g^{-1}$ due to the high-temperature treatment (1150 °C) required for its synthesis. The 0.25-NaTa with a large quantity of amorphous network and small fraction of crystalline $NaTaO_3$ nanoparticles has a surface area of 236 $m^2$ $g^{-1}$, providing a high number of active sites for photocatalysis on the surface. Furthermore, SS-$NaTaO_3$ possess large particles where charge carriers have a long diffusion path to come to the surface, whereas in 0.25-NaTa, an amorphous network and nanoparticles present short diffusion paths for charge carriers, which is known to be beneficial for photocatalysis.

## CONCLUSION

In summary, we report the fabrication of a series of sodium tantalates via a facile hydrothermal synthesis by mixing sodium and tantalum ethoxide precursor in ethanol and adding defined volumes of ammonium hydroxide solution as mineralizer. By controlling the amount of the mineralizer, the morphology, surface area, band gap, and photocatalytic activity toward hydrogen production of the samples were tuned. Sodium tantalum oxide that was prepared with 0.25 mL of $NH_4OH$ solution indicated two band gaps that were assigned to the amorphous structure and a minor fraction of crystalline $NaTaO_3$ nanoparticles. This sample showed the highest hydrogen production rate of 3.6 mmol $h^{-1}$ after 2 h and 3.0 mmol $h^{-1}$ after 48 h using methanol as a sacrificial agent and 94 $\mu$mol $h^{-1}$ during overall water splitting. Despite the amorphous structure, this material showed much better photocatalytic performance by reaching an apparent photocatalytic activity of 1200 $\mu$mol $g^{-1}$ $L^{-1}$ $h^{-1}$ $W^{1-}$ that is about 4.5-times higher than that displayed by crystalline SS-$NaTaO_3$. These results show that amorphous network-like morphologies have great potential for the production of clean hydrogen via photocatalytic water splitting.

## ASSOCIATED CONTENT

### Supporting Information

The Supporting Information is available free of charge on the ACS Publications website at DOI: 10.1021/acsami.5b06965.

TEM images of reference $NaTaO_3$, XPS spectra of Ta 4f and Na 1s binding energies of 0.25-NaTa and 0-NaTa, diagram of the measured pressure during hydrothermal synthesis in dependence of the amount of ammonium hydroxide solution, XRD pattern of 0-NaTa prepared at 90 bar pressure, UV−vis diffuse reflectance spectra of the sodium tantalate series, and 48 h hydrogen production rate of 0.25-NaTa with XRD, and TEM study from before and after (PDF)

## AUTHOR INFORMATION

### Corresponding Author

*E-mail: tueysuez@kofo.mpg.de.

### Notes

The authors declare no competing financial interest.

## ACKNOWLEDGMENTS

We thank Prof. C. Chan (Arizona State University) for discussion; Dr. C. Weidenthaler for XPS analyses, discussion, and support for Scherrer calculation; and our TEM department for images and EDX analysis. In addition, we thank MAXNET Energy Research Network of the Max-Planck-Society, Cluster of Excellence RESOLV (EXC 1069) funded by the Deutsche Forschungsgemeinschaft (DFG) and Fonds der Chemischen Industrie (FCI) for funding. T.G. thanks FCI for a Chemiefonds Fellowship.

## REFERENCES

(1) Fresno, F.; Portela, R.; Suarez, S.; Coronado, J. M. Photocatalytic Materials: Recent Achievements and Near Future Trends. *J. Mater. Chem. A* **2014**, *2*, 2863−2884.

(2) Gray, H. B. Powering the Planet with Solar Fuel. *Nat. Chem.* **2009**, *1*, 7−7.

(3) Osterloh, F. E. Inorganic Materials as Catalysts for Photochemical Splitting of Water. *Chem. Mater.* **2008**, *20*, 35−54.

(4) Takanabe, K.; Domen, K. Preparation of Inorganic Photocatalytic Materials for Overall Water Splitting. *ChemCatChem* **2012**, *4*, 1485−1497.



DOI: 10.1021/acsami.5b06965
*ACS Appl. Mater. Interfaces* 2015, 7, 23153−23162

(5) Zhang, P.; Zhang, J.; Gong, J. Tantalum-Based Semiconductors for Solar Water Splitting. *Chem. Soc. Rev.* **2014**, *43*, 4395−4422.
(6) Liu, J. W.; Chen, G.; Li, Z. H.; Zhang, Z. G. Hydrothermal Synthesis and Photocatalytic Properties of ATaO3 and ANbO3 (A = Na and K). *Int. J. Hydrogen Energy* **2007**, *32*, 2269−2272.
(7) Noda, Y.; Lee, B.; Domen, K.; Kondo, J. N. Synthesis of Crystallized Mesoporous Tantalum Oxide and Its Photocatalytic Activity for Overall Water Splitting under Ultraviolet Light Irradiation. *Chem. Mater.* **2008**, *20*, 5361−5367.
(8) Hu, C.-C.; Teng, H. Influence of Structural Features on the Photocatalytic Activity of NaTaO3 Powders from Different Synthesis Methods. *Appl. Catal., A* **2007**, *331*, 44−50.
(9) Li, Y.; Gou, H.; Lu, J.; Wang, C. A Two-Step Synthesis of $NaTaO_3$ Microspheres for Photocatalytic Water Splitting. *Int. J. Hydrogen Energy* **2014**, *39*, 13481−13485.
(10) Kato, H.; Kudo, A. Water Splitting into H2 and O2 on Alkali Tantalate Photocatalysts ATaO3 (A = Li, Na, and K). *J. Phys. Chem. B* **2001**, *105*, 4285−4292.
(11) Zhang, M.; Liu, G.; Zhang, D.; Chen, Y.; Wen, S.; Ruan, S. Facile Fabrication of NaTaO3 Film and its Photoelectric Properties. *J. Alloys Compd.* **2014**, *602*, 322−325.
(12) Kato, H.; Asakura, K.; Kudo, A. Highly Efficient Water Splitting into H2 and O2 over Lanthanum-Doped NaTaO3 Photocatalysts with High Crystallinity and Surface Nanostructure. *J. Am. Chem. Soc.* **2003**, *125*, 3082−3089.
(13) Tüysüz, H.; Schüth, F. Ordered Mesoporous Materials as Catalysts. *Adv. Catal.* **2012**, *55*, 127−239.
(14) Wang, P.; Chen, P.; Kostka, A.; Marschall, R.; Wark, M. Control of Phase Coexistence in Calcium Tantalate Composite Photocatalysts for Highly Efficient Hydrogen Production. *Chem. Mater.* **2013**, *25*, 4739−4745.
(15) Marschall, R. Semiconductor Composites: Strategies for Enhancing Charge Carrier Separation to Improve Photocatalytic Activity. *Adv. Funct. Mater.* **2014**, *24*, 2421−2440.
(16) Kho, Y. K.; Iwase, A.; Teoh, W. Y.; Mädler, L.; Kudo, A.; Amal, R. Photocatalytic H2 Evolution over TiO2 Nanoparticles: the Synergistic Effect of Anatase and Rutile. *J. Phys. Chem. C* **2010**, *114*, 2821−2829.
(17) Kim, H. G.; Borse, P. H.; Jang, J. S.; Jeong, E. D.; Jung, O.-S.; Suh, Y. J.; Lee, J. S. Fabrication of CaFe2O4/MgFe2O4 Bulk Heterojunction for Enhanced Visible Light Photocatalysis. *Chem. Commun.* **2009**, 5889−5891.
(18) Fu, X.; Wang, X.; Leung, D. Y. C.; Xue, W.; Ding, Z.; Huang, H.; Fu, X. Photocatalytic Reforming of Glucose over La Doped Alkali Tantalate Photocatalysts for H2 Production. *Catal. Commun.* **2010**, *12*, 184−187.
(19) Xu, J.; Xue, D.; Yan, C. Chemical Synthesis of NaTaO3 Powder at Low-Temperature. *Mater. Lett.* **2005**, *59*, 2920−2922.
(20) Kato, H.; Kudo, A. New Tantalate Photocatalysts for Water Decomposition into H2 and O2. *Chem. Phys. Lett.* **1998**, *295*, 487−492.
(21) Aguas, M. D.; Parkin, I. P. Combined Combustion Sol-Gel Synthesis of LiNbO3, LiTaO3, NaNbO3 and NaTaO3. *J. Mater. Sci. Lett.* **2001**, *20*, 57−58.
(22) Li, X.; Zang, J. Facile Hydrothermal Synthesis of Sodium Tantalate (NaTaO3) Nanocubes and High Photocatalytic Properties. *J. Phys. Chem. C* **2009**, *113*, 19411−19418.
(23) Grewe, T.; Meier, K.; Tüysüz, H. Photocatalytic Hydrogen Production over Various Sodium Tantalates. *Catal. Today* **2014**, *225*, 142−148.
(24) Maeda, K.; Terashima, H.; Kase, K.; Domen, K. Nanoparticulate Precursor Route to Fine Particles of TaON and ZrO2−TaON Solid Solution and Their Photocatalytic Activity for Hydrogen Evolution under Visible Light. *Appl. Catal., A* **2009**, *357*, 206−212.
(25) Takahara, Y.; Kondo, J. N.; Takata, T.; Lu, D.; Domen, K. Mesoporous Tantalum Oxide. 1. Characterization and Photocatalytic Activity for the Overall Water Decomposition. *Chem. Mater.* **2001**, *13*, 1194−1199.
(26) Nakajima, K.; Hara, M.; Domen, K.; Kondo, J. N. Synthesis of Highly Ordered Mesoporous Tantalum Oxide. *Chem. Lett.* **2005**, *34*, 394−395.
(27) Yokoi, T.; Sakuma, J.; Maeda, K.; Domen, K.; Tatsumi, T.; Kondo, J. N. Preparation of a Colloidal Array of NaTaO3 Nanoparticles via a Confined Space Synthesis Route and its Photocatalytic Application. *Phys. Chem. Chem. Phys.* **2011**, *13*, 2563−2570.
(28) Tüysüz, H.; Chan, C. K. Preparation of Amorphous and Nanocrystalline Sodium Tantalum Oxide Photocatalysts with Porous Matrix Structure for Overall Water Splitting. *Nano Energy* **2013**, *2*, 116−123.
(29) Kang, H. W.; Kim, E.-J.; Park, S. B. Preparation of NaTaO3 by Spray Pyrolysis and Evaluation of Apparent Photocatalytic Activity for Hydrogen Production from Water. *Int. J. Photoenergy* **2008**, *2008*, 8.
(30) Scherrer, P. Bestimmung der Grösse und der Inneren Struktur von Kolloidteilchen Mittels Röntgenstrahlen. *Nachr. Ges. Wiss. Göttingen, Math.-Phys. Kl.* **1918**, *26*, 98−100.
(31) Langford, J. I.; Wilson, A. J. C. Scherrer after sixty years: A survey and some new results in the determination of crystallite size. *J. Appl. Crystallogr.* **1978**, *11*, 102−113.
(32) Weidenthaler, C. Pitfalls in the Characterization of Nanoporous and Nanosized Materials. *Nanoscale* **2011**, *3*, 792−810.
(33) Marschall, R. Heterojunctions in Composite Photocatalysts. *Top. Curr. Chem.* **2015**, DOI: 10.1007/128_2015_636.
(34) Huang, L.; Chan, Q.; Zhang, B.; Wu, X.; Gao, P.; Jiao, Z.; Liu, Y. Preparation of Sodium Tantalate with Different tructures and Its Photocatalytic Activity for H2 Evolution from Water Splitting. *Chin. J. Catal.* **2011**, *32*, 1822−1830.
(35) Grewe, T.; Tüysüz, H. Designing Photocatalysts for Hydrogen Evolution: Are Complex Preparation Strategies Necessary to Produce Active Catalysts? *ChemSusChem* **2015**, *8*, 3084−3091.
(36) Lin, W.-H.; Cheng, C.; Hu, C.-C.; Teng, H. NaTaO3 Photocatalysts of Different Crystalline Structures for Water Splitting into H2 and O2. *Appl. Phys. Lett.* **2006**, *89*, 211904.
(37) Kudo, A.; Kato, H.; Tsuji, I. Strategies for the Development of Visible-light-driven Photocatalysts for Water Splitting. *Chem. Lett.* **2004**, *33*, 1534−1539.
(38) Reitz, C.; Brezesinski, K.; Haetge, J.; Perlich, J.; Brezesinski, T. Nanocrystalline NaTaO3 Thin Film Materials with Ordered 3D Mesoporous and Nanopillar-like Structures through PIB-b-PEO Polymer Templating: Towards High-Performance UV-Light Photocatalysts. *RSC Adv.* **2012**, *2*, 5130−5133.
(39) Ikeda, S.; Fubuki, M.; Takahara, Y. K.; Matsumura, M. Photocatalytic Activity of Hydrothermally Synthesized Tantalate Pyrochlores for Overall Water Splitting. *Appl. Catal., A* **2006**, *300*, 186−190.
(40) Kudo, A.; Miseki, Y. Heterogeneous Photocatalyst Materials for Water Splitting. *Chem. Soc. Rev.* **2009**, *38*, 253−278.
(41) Iwasita, T. Methanol and CO Electrooxidation. In *Handbook of Fuel Cells: Fundamentals, Technology, Applications*; Vielstich, W., Gasteiger, H. A., Lamm, A., Eds.; Wiley: Hoboken, NJ, 2003; Vol. *2*, pp 603−624.
(42) Ferrin, P.; Nilekar, A. U.; Greeley, J.; Mavrikakis, M.; Rossmeisl, J. Reactivity Descriptors for Direct Methanol Fuel Cell Anode Catalysts. *Surf. Sci.* **2008**, *602*, 3424−3431.
(43) Chen, X.; Shen, S.; Guo, L.; Mao, S. S. Semiconductor-based Photocatalytic Hydrogen Generation. *Chem. Rev.* **2010**, *110*, 6503−6570.
(44) Chou, H.-L.; Hwang, B.-J.; Sun, C.-L. Chapter 9—Catalysis in Fuel Cells and Hydrogen Production. In *New and Future Developments in Catalysis*; Suib, S. L., Ed.; Elsevier: Amsterdam, 2013; pp 217−270.
(45) Law, M.; Greene, L. E.; Radenovic, A.; Kuykendall, T.; Liphardt, J.; Yang, P. ZnO−Al2O3 and ZnO−TiO2 Core−Shell Nanowire Dye-Sensitized Solar Cells. *J. Phys. Chem. B* **2006**, *110*, 22652−22663.
(46) Guo, S.; Han, S.; Mao, H.; Dong, S.; Wu, C.; Jia, L.; Chi, B.; Pu, J.; Li, J. Structurally Controlled ZnO/TiO2 Heterostructures as Efficient Photocatalysts for Hydrogen Generation from Water without


DOI: 10.1021/acsami.5b06965
*ACS Appl. Mater. Interfaces* 2015, 7, 23153−23162

Noble Metals: The Role of Microporous Amorphous/Crystalline Composite Structure. *J. Power Sources* **2014**, *245*, 979−985.
(47) Tan, H.; Zhao, Z.; Niu, M.; Mao, C.; Cao, D.; Cheng, D.; Feng, P.; Sun, Z. A Facile and Versatile Method for Preparation of Colored TiO2 with Enhanced Solar-Driven Photocatalytic Activity. *Nanoscale* **2014**, *6*, 10216−10223.
(48) He, W.; Yang, Y.; Wang, L.; Yang, J.; Xiang, X.; Yan, D.; Li, F. Photoelectrochemical Water Oxidation Efficiency of a Core/Shell Array Photoanode Enhanced by a Dual Suppression Strategy. *ChemSusChem* **2015**, *8*, 1568−1576.
(49) Kim, H.-i.; Monllor-Satoca, D.; Kim, W.; Choi, W. N-doped TiO2 Nanotubes Coated with a Thin TaOxNy Layer for Photoelectrochemical Water Splitting: Dual Bulk and Surface Modification of Photoanodes. *Energy Environ. Sci.* **2015**, *8*, 247−257.
(50) Yang, J.; Wang, D.; Han, H.; Li, C. Roles of Cocatalysts in Photocatalysis and Photoelectrocatalysis. *Acc. Chem. Res.* **2013**, *46*, 1900−1909.
(51) Grewe, T.; Meggouh, M.; Tüysüz, H. Nanocatalysts for Solar Water Splitting and a Perspective on Hydrogen Economy. *Chem. - Asian J.* **2015**, DOI: 10.1002/asia.201500723.


DOI: 10.1021/acsami.5b06965
*ACS Appl. Mater. Interfaces* 2015, 7, 23153−23162